Available online at www.sciencedirect.com
ScienceDirect
Journal of the European Ceramic Society 31 (2011) 2043–2056
www.elsevier.com/locate/jeurceramsoc

A model for the C-A-S-H gel formed in alkali-activated slag cements

F. Puertas[a,b,*], M. Palacios[c], H. Manzano[d,e], J.S. Dolado[d,b], A. Rico[f], J. Rodríguez[f]

[a] *Instituto de Ciencias de la Construcción Eduardo Torroja (IETcc-CSIC), Madrid, Spain*
[b] *Nanostructured and Eco-efficient Materials for Construction Unit, Associated Unit Labein-Tecnalia/CSIC.IETcc, Spain*
[c] *Institute for Building Materials-ETH Zurich, Switzerland*
[d] *Labein-Tecnalia, Derio, Bilbao, Spain*
[e] *Concrete Sustainability Hub, Massachusetts Institute of Technology, Cambridge, MA, USA*
[f] *Universidad Rey Juan Carlos, Móstoles, Madrid, Spain*

Received 16 December 2010; received in revised form 11 April 2011; accepted 30 April 2011
Available online 24 May 2011

Abstract

For first time, an experimental and computational study has been conducted to define a structural model for the C-A-S-H gel forming in alkali-activated slag (AAS) pastes that would account for the mechanical properties of these materials. The study involved a comparison with the C-S-H gel forming in a Portland cement paste.

The structure of the C-A-S-H gels in AAS pastes depends on the nature of the alkali activator. When the activator is a NaOH, the structure of the C-S-H gel falls in between tobermorite 1.4 nm with a mean chain length of five, and tobermorite 1.1 nm with a mean length of 14. When waterglass is the activator the structure of the C-A-S-H gel is indicative of the co-existence of tobermorite 1.4 nm with a chain length of 11 and tobermorite 1.1 nm with a chain length of 14. This very densely packed structure gives rise to excellent mechanical properties.

Keywords: Microstructure-final; Spectroscopy; Mechanical properties; Atomistic modelling; Cements

1. Introduction

Alkali-activated slag (AAS) cement development has been the object of much research in recent years because of the energy and environmental advantages of its production over ordinary Portland cement (OPC) manufacture. Specifically, the development of these alkaline cements entails the re-use of industrial waste, the reduction of both energy consumption and a substantial decline in greenhouse gas emissions, essentially CO_2. These cements are obtained by mixing vitreous granulated blast furnace slag with highly basic solutions such as waterglass ($Na_2O{\cdot}nSiO_2{\cdot}mH_2O + NaOH$), NaOH or Na_2CO_3, among others. In terms of mechanical properties, AAS cements are comparable to OPC, particularly when waterglass is used as the activating solution.[1,2] At the same time, they exhibit greater durability when exposed to acid, sulphates or seawater than Portland cement systems.[3–5] Earlier studies[6–8] have shown, however, that AAS cements and concretes carbonate more readily than OPCs, and that one of the chief technological problems posed by these alkaline materials when waterglass is the activating solution is their high autogenous and drying shrinkage rate. When NaOH or Na_2CO_3, solutions are used, however, cement shrinkage is comparable to the rate observed in OPC.[9]

The properties exhibited by alkaline cements and concretes are directly related to the nature and structure of their main reaction product, C-A-S-H gel. Further to the literature,[10,2,11] the C-A-S-H gel forming in AAS pastes, like the C-S-H gel in OPC pastes,[12] is made up of tetrahedrally coordinated silicate chains with a dreierkette structure, in which each chain consists of $(3n-1)$ tetrahedra. The C-A-S-H gel chains in AAS cements are longer (with up to 13 tetrahedra) than the C-S-H gel chains in OPC systems (three to five tetrahedra) and, unlike the latter, include aluminium in their structure, which replaces the silicon in bridging positions. This substitution of Al^{3+} for Si^{4+} generates a charge imbalance compensated by the uptake of Na^+ ions in the gel. On the grounds of MAS NMR and BSE/EDX findings, a number of researchers[10,2,11] have concluded that the nature of the alkaline activator used leads to differences in C-A-S-H gel structure and composition in these AAS cements.

* Corresponding author at: Instituto de Ciencias de la Construcción Eduardo Torroja (IETcc-CSIC), Madrid, Spain.
E-mail address: puertasf@ietcc.csic.es (F. Puertas).

0955-2219/$ – see front matter © 2011 Elsevier Ltd. All rights reserved.
doi:10.1016/j.jeurceramsoc.2011.04.036

Fernández-Jiménez et al. and Brough and Atkinson[10,2] reported that the use of waterglass as an alkali activator induces the formation of a C-A-S-H gel with high Si Q^2 and Q^3 or Q^{Poly} contents and the formation of long, intertwined chains. Fernández-Jiménez et al.[10] likewise concluded that when the activator used is a NaOH solution, the C-A-S-H gel exhibits a high Si Q^2 unit content. These authors confirmed the formation of long linear chains with no Si Q^3 units which they did, however, detect in the C-A-S-H gel when using Na_2CO_3 as the activating solution. Finally, this effect of the nature of the alkaline activator on C-A-S-H gel structure has been confirmed to induce differences in its chemical composition.[13] To this respect, Ca/Si in C-A-S-H gel in AAS is substantially smaller than the C-S-H gel in OPC systems.

While atomistic simulation techniques have recently been used to describe the structure and properties of C-S-H gel in OPCs,[14–16] they have not yet to be applied to analyse AAS. The present study for first time a combination of experimental and modern computational techniques to propose a new model for C-A-S-H gels found in waterglass- and NaOH-activated AAS cements. A structural comparison between the C-A-S-H and C-S-H gels is provided to facilitate the description.

2. Experimental

2.1. Materials, paste preparation and trials

Table 1 gives the chemical composition of the blast furnace slag and type 42.5R I Portland cement used. The specific surface values for the slag and the Portland cement were 325 and 360 m^2/kg, respectively; the vitreous phase content of the former was 99%.

AAS and OPC pastes were prepared with liquid/solid ratios of 0.5 and 0.4, respectively. Two alkaline solutions were used for the alkali-activated slag pastes: waterglass and NaOH, with a Na_2O content of 4% of the slag weight. After 28-day storage in humidity chamber (98% RH, $20 \pm 2\,^{\circ}C$), the AAS and OPC pastes were tested as described below.

Mineralogy and microstructure: ground samples were characterised using several techniques:

a) *Fourier transform infrared (FTIR) spectroscopy*. An ATI-MATTSON Genesis series FTIR-TM spectrometer was used. The solid samples were prepared by press-forming pellets containing approximately 1.0 mg of sample and 300 mg of KBr.
b) *^{29}Si and ^{27}Al magic angle solid nuclear magnetic resonance* (*MAS NMR*). A BRUKER MSL 400 spectrometer was used. The ^{29}Si and ^{27}Al spectra were obtained at resonance frequencies of 79.49 and 104.2 MHz, respectively. Chemical shift values were found using tetramethylsilane (TMS) and a 1-M solution of $AlCl_3{\cdot}Cl_3{\cdot}6H_2O$ as standards for ^{29}Si and ^{27}Al, respectively.
c) *Back-scattering scanning electron microscopy* (*BSE/EDX*). A JOEL 5400 microscope fitted with an Oxford-Link ISIS EDX microanalysis unit was used. The samples were embedded in epoxy resin, cut, polished and carbon coated.

Mechanical characterisation with nanoindentation trials. These trials were conducted on 28-day paste samples prepared and cured as described above, and subsequently cut and polished. Depth sensing indentation tests were conducted on an MTS System Co. XP nanoindenter fitted with a 100-nm nominal edge radius Berkovich tip. The load was applied with a 50-nN calibrated electromagnetic coil. Indenter displacement was measured using a capacitive transducer with a resolution of 0.01 nm. The experiment set-up described by Constantinides et al.[17] was followed. Accordingly, an indentations matrix (17×15 indentations spaced at 5-μm intervals) was formed on a representative area of the samples. Indentation loads of 300 and 500 μN were used. The Young's modulus and sample hardness were estimated for each indentation from the load–displacement curve using the procedure described by Oliver and Pharr for a Berkovich tip.

3. Computational method

Atomistic simulations were performed with the force field method. In this approach, atoms are described as spheres with characteristic charges and sizes, and the interaction between electrons and nucleus is defined by a set of parameterised empirical potentials fitted to the experimental data or *ab initio* simulations.[18] The potential set for calcium silicate hydrates taken from the literature[19–21] for the present study had been checked in prior research on the mechanical properties of crystalline calcium silicates[22,23] and the main phases in cement pastes. The set was enlarged in the present study to include Al and Na. As in the case of silicon and calcium, the derived potentials for aluminium and sodium are described in Gale et al.[24] and Higgins et al.[25] A Buckingham (two-body) potential function was chosen for the Al–O and Na–O short-range interactions and a three-body harmonic (O–Al–O) for tetrahedral coordination. The species and parameters described in this paper are given in Table 2.

The starting structures for the simulations were jennite and the anomalous 1.1- and 1.4-nm varieties of tobermorite.[26,27] Jennite and tobermorite consist of layers of Ca–O flanked on both sides by chains of silicates. In tobermorite, all the Ca atoms in this layer are linked to the silicate chains, while in jennite the amount of Ca in the layer is higher and some Ca atoms are partially coordinated to hydroxyl group. Within the tobermorite family, the difference arise form the interlaminar space structure and conection between sheets. While in tobermorite 1.4 nm two consecutive layers are connected by interlaminar Ca atoms forming SiO–Ca–OSi ionic bonds, the silicate chains of tobermorite 1.1 nm are connected by a Si–O–Si covalent bond. Starting from the perfect models, certain silicon atoms in tobermorite were replaced with aluminium atoms to study the effect of the latter on the elastic properties of the mineral. The Si replaced was the atom in the bridging site, identified by experimental and theoretical evidence to be the most probable position for this substitution.[28–33] The charge imbalance generated by Al uptake was compensated by including Na^+ ions in the interlam-

Table 1
Chemical composition of blast furnace slag and cement.

% wt	CaO	SiO_2	Al_2O_3	MgO	Fe_2O_3	SO_3	S^{2-}	Na_2O	K_2O	L.O.I.	I.R.
Slag	41.37	34.95	13.11	7.12	0.69	0.04	1.92	0.27	0.23	2.02	0.11
OPC	64.41	17.91	5.17	1.30	3.85	2.64	–	0.39	0.78	0.78	0.29

L.O.I. = loss on ignition; I.R. = insoluble residue.

Table 2
Parameters employed to describe the atomic interactions in the C-S-H systems. The letter following the atoms distinguishes the oxygen and hydrogen atoms according to their nature: water (w), hydroxyl groups (oh). Two different calcium atoms are considered, the one in the Ca-O layers (inter) and the one in the interlaminar space (intra). For non-laminar CSH crystals the Ca inter parameters were employed. *Continues in the next page.*

Species	Charge core	Charge shell	Spring K (eV Å^{-2})	Reference
Ca inter	2.00	–		47
Ca intra	2.00	–		47
Na	1.00			
Ow	1.25	−2.050	209.00	48
Ooh	0.87	−2.270	74.90	21
Hoh	0.40	–		21
Hw	0.40	–		48
Si	4.00	–		49
Al	3.00	–		24

Buckingham	A (eV)	ρ (Å)	C (eV A^6)	Cut off (Å)	
Ca inter–Osi	1090.000	0.3440	0.00	12.0	47
Ca inter–Ooh	777.000	0.3440	0.00	12.0	47
Ca inter–Ow	777.000	0.3440	0.00	12.0	47
Ca intra–Osi	1090.000	0.3440	0.00	12.0	47
Ca intra–Ooh	1090.000	0.3440	0.00	12.0	47
Ca intra–Ow	777.000	0.3440	0.00	12.0	47
Na–Osi	1271.504	0.300	0.00	12.0	25
Na–Ooh	1271.504	0.300	0.00	12.0	25
Na–Ow	1271.504	0.300	0.00	12.0	25
Si–Osi	1283.907	0.3205	10.66158	12.0	49
Si–Ooh	983.557	0.3205	10.66158	12.0	49
Si–Ow	984.000	0.3210	10.66158	12.0	21
Al–Osi	1142.678	0.2991	0.00	12.0	24
Al–Ow	1142.678	0.2991	0.00	12.0	24
Al–Ooh	1142.678	0.2991	0.00	12.0	24
Osi–Osi	22800.000	0.3210	27.90	12.0	49
Osi–Ooh	22800.000	0.1490	13.90	12.0	49
Osi–Ow	22800.000	0.1490	0.149	12.0	21
Ooh–Ooh	22800.000	0.1490	6.970	12.0	49
Ooh–Ow	22800.000	0.1490	0.149	12.0	21
Ooh–Hw	312.000	0.2500	0.00	12.0	21
Ow–Hw	396.000	0.2500	0.00	12.0	48
Ow–Hoh	312.000	0.2500	0.00	12.0	21

Morse	D (eV)	α (Å^{-2})	r_0 (Å)	Cut off (Å)	
O–H	7.050	3.170	0.943	1.400	21

Lennard Jones	A (eV Å^{-6})	B (eV Å^{-12})	Cut off (Å)	
Ow–Ow	39300.00	42.10	12.0	48

Three body harmonic	k (eV rad^{-2})	θ_0 (°)	Cut off 1-2-3 (Å)	
Si–Osi–Osi	2.097	109.470	1.8/1.8/3.2	49
Si–Osi–Ooh	2.097	109.470	1.8/1.8/3.2	49
Al–Osi–Osi	2.097	109.470	1.8/1.8/3.2	24
Al–Osi–Ooh	2.097	109.470	1.9/1.9/3.5	24

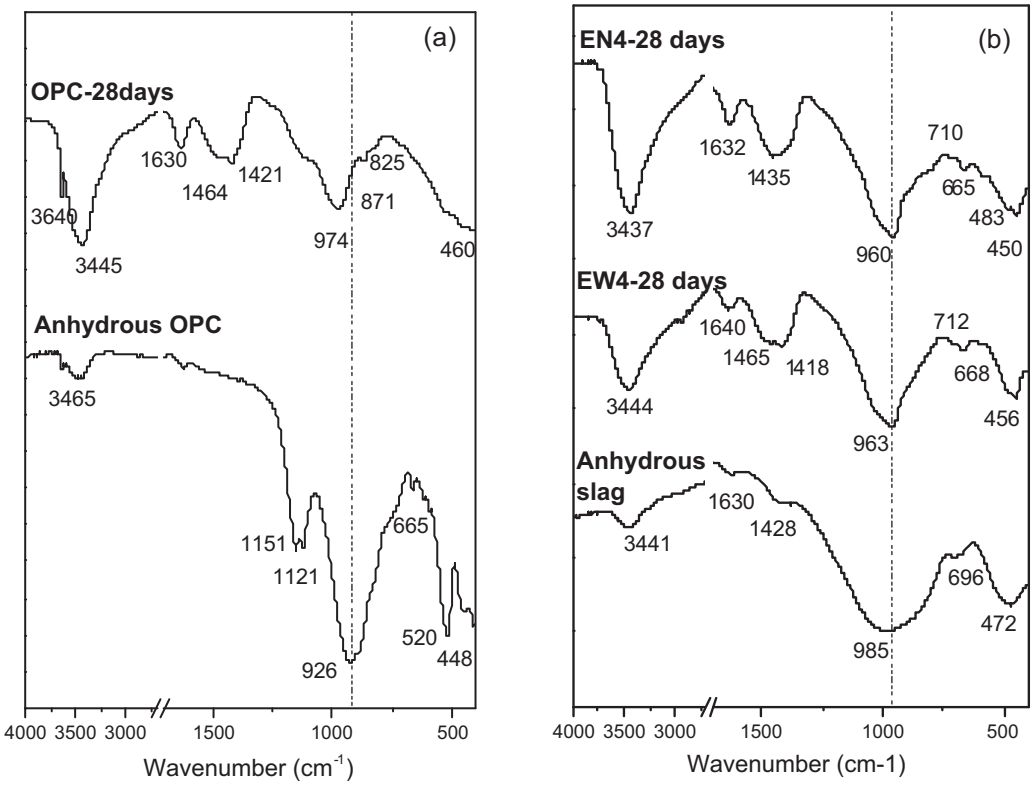

Fig. 1. FTIR spectra for 28-day pastes: (a) cement and (b) waterglass- and NaOH-activated slag.

inar space at an Al/Na ratio of 1. The sodium atoms were placed in the interlaminar space, at an intial distance of ~3.5 Å from the aluminium site, with a random angle around the on the z axis of the crystal. Si was replaced by Al randomly, and various configurations and aluminosilicate chain lengths were tested to find the Al/Si ratio closest to the experimental ratio of ~0.18. The number of bridging tetrahedra was reduced as necessary to build finite chains from infinite crystals, inasmuch as this defect has been suggested as the reason for the appearance of finite chains in cement pastes. The finite chains were constructed by omission of the bridging silicate tetrehedra. In tobermorite 14 Å, one has to remove a silicon atom (+4), an oxygen (−2) and an OH group (−1). With this procedure, the system gains one electron. To return the unit cell to its neutral state, the extra charge has been compensated by saturating half of the dangling oxygen atoms of silicate chains with H so that they form terminal OH groups. In the case of tobermorite 11 A, the bridging silicates removed are linked, so each time we detach 2 Si^{4+}, and 3 O^{-2}. The charge imbalance is then (−2), and all the dangling O atoms were saturated with hydrogen. The silicate chain lengths studied ranged from 2 to 5 in jennite, 2 to 11 in tobermorite 1.4 nm and 2 to 14 in tobermorite 1.1 nm.

The GULP code[34] was used to perform the calculations. In this approach, the initial structures are optimized to the local energy values that minimise lattice energy, while allowing cell parameters and atomic positions to vary. A Cuasi–Newton–Rapshon minimisation procedure, an update of the Hessian variation on the Broyden–Fletcher–Goldfarb–Shannon (BFGS) scheme, was used. The elastic matrix coefficients were then calculated from the second derivatives of the energy around the minimum energy in the relaxed structures. The Hill definition bulk (K) and shear (G) moduli were calculated from the elastic matrix. C-A-S-H gel porosity was factored into the model at this stage, re-scaling the values of the bulk tobermorite crystals as per existing micromechanical models. The self-consistent model has proven to be the best approach for describing C-S-H gel to date. This model was developed to find the elasticity of a granular medium consisting of spherical particles of different sizes, given the elastic properties of these components.[35] After rescaling the bulk and shear moduli, the anisotropic Youngs modulus (E) and Poisson's ratio (μ) can be calculated trough the relationships:

$$E = \frac{9G}{3 + G/K}$$

$$v = \frac{3 - 2}{6 + 2G/K}$$

The anisotrpic values compare better with the nanoindentation measurements, as this experimental technique give us average values over all the possible orientations rather than in a specific direction.

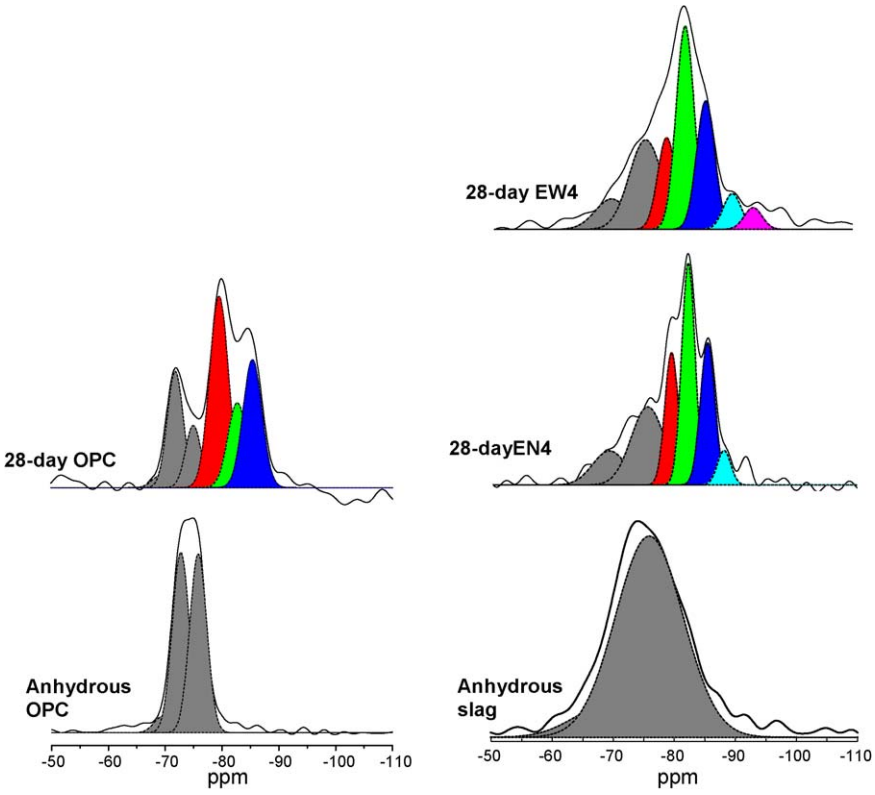

Fig. 2. ^{29}Si MAS NMR spectra for 28-day pastes: waterglass- and NaOH-activated slag and Portland cement.

Table 3
^{29}Si MAS NMR signal deonvolution values for 28-day Portland cement and waterglass- and NaOH-activated slag pastes.

Paste	Q^1 (anhydrous)			Q^1 (end of chain)	Q^2 (1Al) and Q^{2B}	Q^2	Q^3 (1Al)	Q^3
OPC—28 days	−68.0 ppm	−71.6 ppm	−75.0 ppm	−79.5 ppm	−83.0 ppm	−85.3 ppm		
	W = 3.70	W = 3.70	W = 3.70	4.02	4.02	4.02		
	I = 2.3%	I = 20.0%	I = 10.3%	35.5%	12.3%	19.6%		
EW—28 days	−69.7 ppm		−75.4 ppm	−78.9 ppm	−82.0 ppm	−85.4 ppm	−89.9 ppm	−93.4 ppm
	W = 7.40		W = 7.40	3.50	3.50	3.50	3.50	3.50
	I = 7.6%		I = 26.6%	12.6%	28.7%	17.9%	4.3%	2.3%
EN—28 days	−69.2 ppm		−75.4 ppm	−79.5 ppm	−82.3 ppm	−85.5 ppm	−88.1 ppm	
	W = 7.00		7.00	2.70	2.70	2.70	2.70	
	I = 9.1%		25.0%	16.1%	28.3%	17.6%	3.9%	

4. Results

4.1. Mineralogical, microstructural and mechanical characterisation

The IR spectrum for OPC pastes (Fig. 1a) contained a narrow band at 3640 cm^{-1} associated with the O–H stretching vibrations in portlandite. Another band was detected at around 974 cm^{-1}, attributed to the stretching vibrations in the Si–O bonds (ν_3(Si–O)) in the SiO_4 tetrahedra that comprise the C-S-H gel, and a third at 460 cm^{-1}, assigned to ν_4(O–Si–O) bending vibrations. The band at around 967–971 cm^{-1} on the IR spectra for NaOH- and waterglass-AAS (Fig. 1b) was associated with the ν_3(Si–O) stretching vibrations in the SiO_4 tetrahedra that

Table 4
BSEM/EDS microanalysis of OPC and AAS pastes.

Paste	Na	Mg	Al	Si	Ca	Ca/Si	Al/Si
OPC	0.26% (±0.12)	0.80% (±0.41)	1.46% (±0.57)	11.79% (±0.71)	25.74% (±1.37)	2.19 (±0.22)	0.12 (±0.05)
EW	6.77% (±2.53)	2.27% (±1.22)	3.98% (±0.64)	15.07% (±1.19%)	15.02% (±3.12%)	0.96 (±0.10)	0.27 (±0.05)
EN	2.00% (±0.79)	4.25% (±1.50)	5.37% (±0.70)	14.18% (± 0.59)	15.30% (± 1.84)	1.10 (±0.11)	0.37 (±0.05)

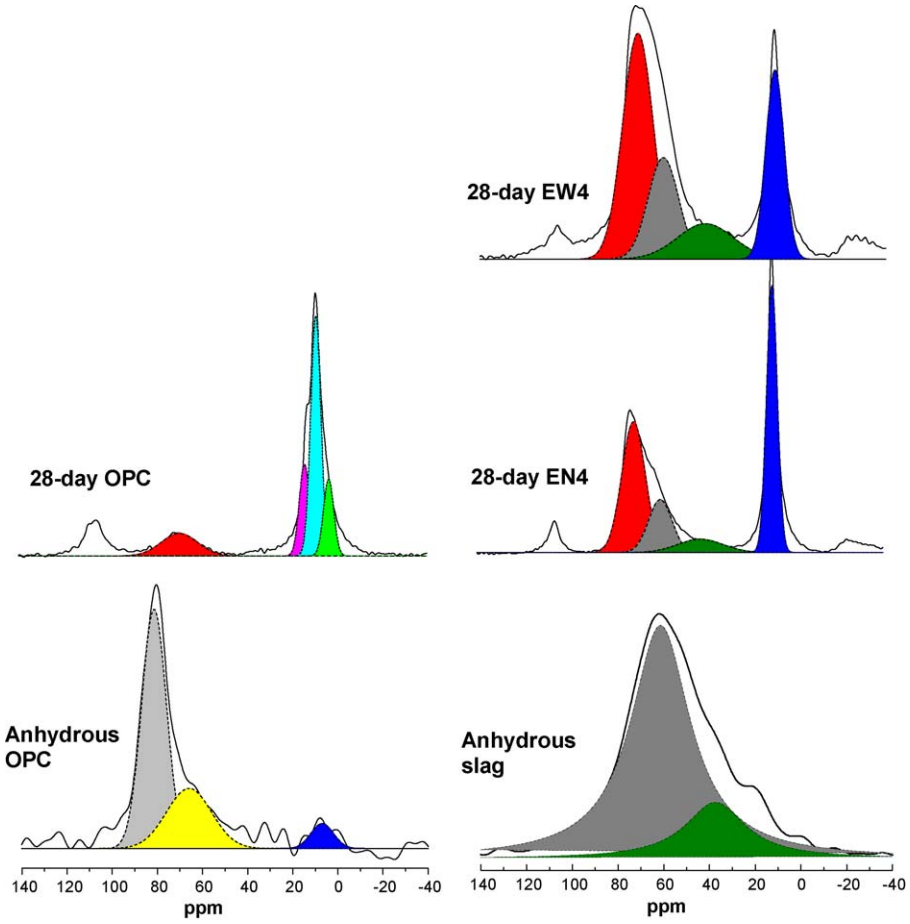

Fig. 3. ^{27}Al MAS NMR spectra for 28-daypastes: waterglass- and NaOH-activated slag and Portland cement.

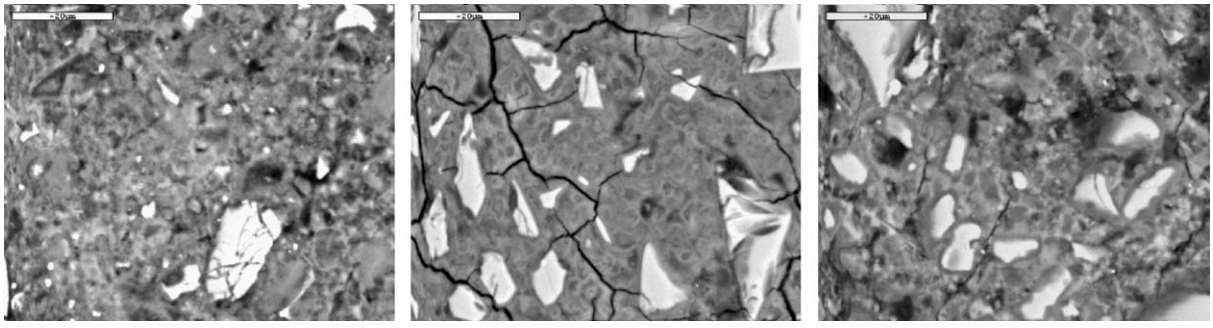

Fig. 4. BSEM images of OPC and waterglass- and NaOH-activated pastes.

Table 5
Data collected from histograms in Fig. 5.

		Young's modulus range (GPa)	Maximum peak value (GPa)	Hardness range (GPa)	Maximum peak value (GPa)
CEM 28d	Distribution A	16–24	19	0.40–0.50	0.45
	Distribution B	25–33	28	0.80–1.00	0.85
	Distribution C	34–44	39	1.20–1.40	1.25
EN 28d	Distribution A	12–20	15	0.30–0.48	0.37
	Distribution B	20–26	23	0.66–0.84	0.73
	Distribution C	35–43	38	1.14–1.32	1.24
EW 28d	Distribution A	28–34	32	0.84–1.00	0.94
	Distribution B	34–40	37	1.08–1.26	1.18
	Distribution C	41–47	44	1.35–1.53	1.43

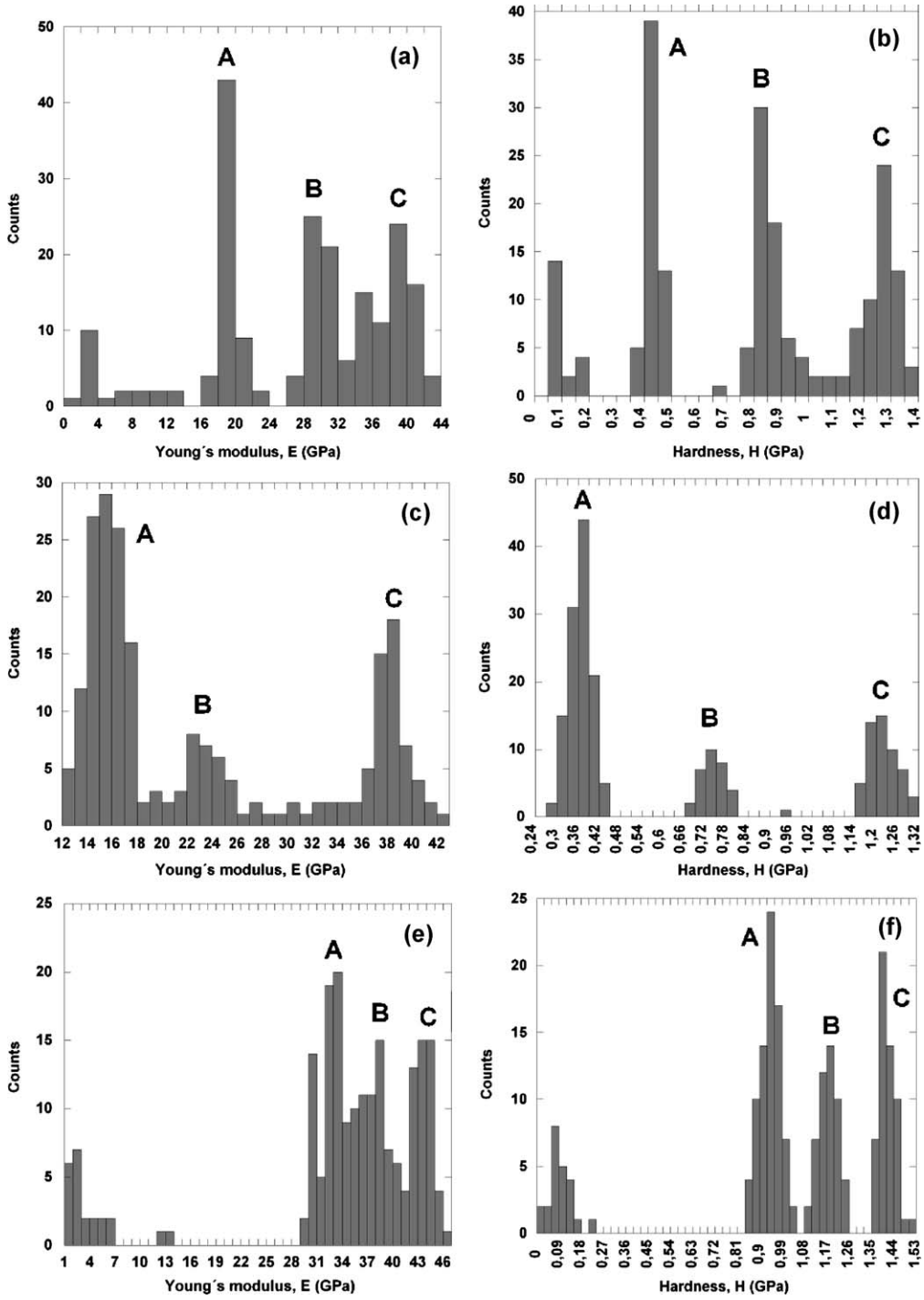

Fig. 5. Hardness and Young's modulus histograms plotted with nanoindentation values: (a) Young's modulus for OPC; (b) hardness for OPC; (c) Young's modulus for EN; (d) hardness for EN; (e) Young's modulus for EW; (f) hardness for EW.

comprise C-A-S-H gel. This ν_3(Si–O) stretching vibration band was narrower in the AAS pastes than in the anhydrous slag, indicating the presence of short-range order in the structure of the gel formed in the AAS pastes. As in OPC pastes, two further bands were attributed to the bending vibrations in the O–Si–O (ν_4(O–Si–O)) bonds, while a band observed at 669 cm^{-1} was assigned to the stretching vibrations in the Al–O bonds in AlO_4 groups. The bands at 3445 and 1630 cm^{-1} detected in the three pastes were associated with the υ_1[OH] and υ_2[OH] bending vibrations in water, respectively. The spectra also contain bands at 1465 and 1420 cm^{-1} attributable to $\nu_3[CO_3]^{2-}$, while the $\nu_2[CO_3]^{2-}$ and $\nu_4[CO_3]^{2-}$ vibration bands detected at 875 and 713 cm^{-1}, respectively, confirmed the carbonation of the pastes.

The ^{29}Si and ^{27}Al MAS NMR spectra for the AAS and OPC pastes are shown in Figs. 2 and 3, respectively, and Table 3 gives the deconvolution data for the ^{29}Si MAS NMR spectra. The MAS NMR spectrum for OPC paste contained three signals at −68.0, −71.6 and −75 ppm attributable to the isolated

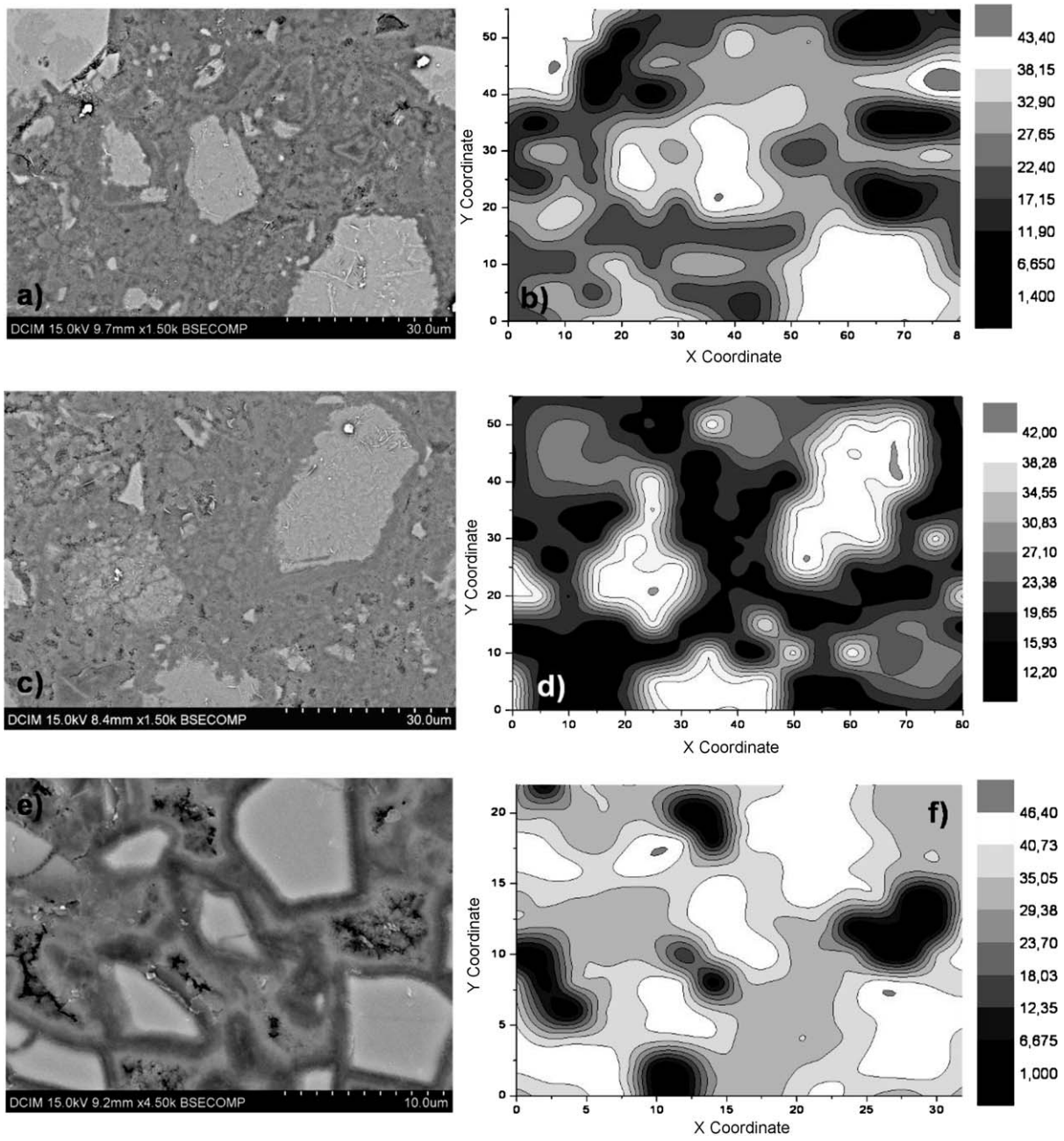

Fig. 6. SEM images showing: (a) a representative portion of the OPC sample; (b) Young's modulus contour map for (a); (c) SEM image showing a representative portion of the EN sample; (d) Young's modulus contour map for (c); (e) SEM image showing a representative portion of the EW sample; (f) Young's modulus contour map for (e).

Q^0 silicate tetrahedra in the clinker (C_3S and C_2S). The signals at −79, −83 and −85 ppm, in turn, were, respectively, assigned to the Q^1, Q^{2B} and Q^2 Si units in the C-S-H gel. The ^{29}Si MAS NMR spectra for the 28-day waterglass- and NaOH-AAS pastes had two signals, at around −69.0 ppm and −75.0 ppm, attributed to the unreacted Q^0 and Q^1 units in the anhydrous slag. A further five signals were detected on the ^{29}Si MAS NMR spectra for the waterglass- and NaOH-AAS, at −78.0, −82.0, −85.0, −89.0 and −93.0 ppm, and, respectively, attributed to Q^1, Q^2 (1Al), and Q^{2B}, Q^3 (1Al) and Q^3 Si units.[10,36] Note that Q^3 Si units were identified in the waterglass—but not in the NaOH-AAS pastes.

The signals on the ^{27}Al MAS NMR spectrum for OPC pastes appeared at: 70 ppm, attributable to the tetrahedral Al present in the anhydrous phases of calcium aluminate, calcium ferroaluminate and alite in the cement clinker; 13.6 ppm, assigned to the octahedral Al in ettringite; 9.0 ppm, attributed to monosulphoaluminate and the unhydrated ferritic phase; 3.3 ppm, associated with the octahedral Al in the hydrated aluminate phases.[37] The ^{27}Al MAS NMR spectra for the NaOH- and waterglass-AAS paste had four signals: ∼70.0 and ∼60.0 ppm, associated with tetrahedral Al units, and ∼40.0 and ∼9.0 ppm, associated with pentahedral and octahedral Al units, respectively.[10,37,38] The

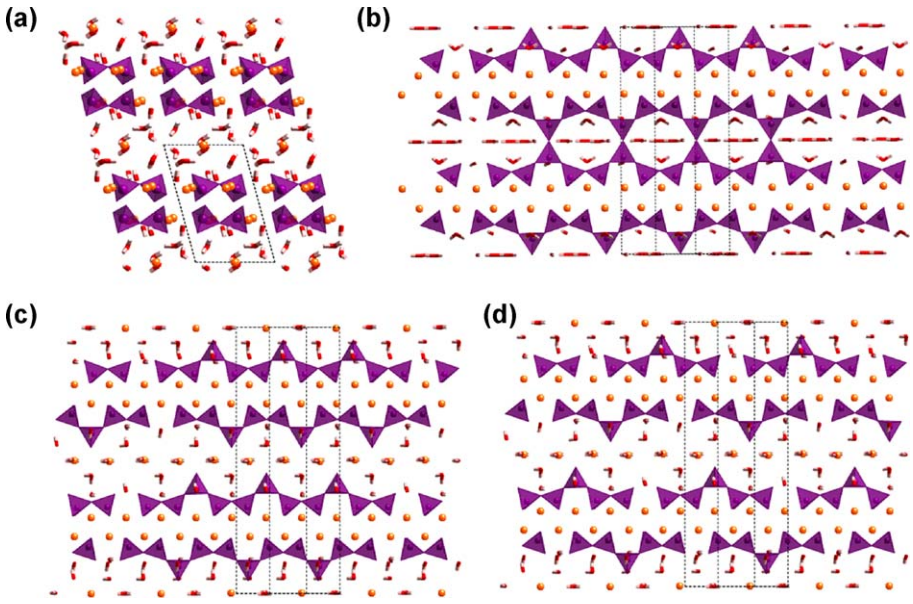

Fig. 7. Structural models for: (a) J2; (b)T11 (14); (c) T14 (11); (d) T14 (5),.

band at around 107 ppm observed the spectra was associated with a rotation band on the central ^{27}Al signal due to the presence of ferromagnetic Fe_3O_4 or antiferromagnetic Fe_2O_3.[39,40]

The SEM/BSE micrographs for the three pastes in Fig. 4 show the difference in their appearance. The white particles are anhydrous cement or vitreous slag grains. The greyish matrix is essentially the C-S-H or C-A-S-H gel. This matrix was observed to be more compact and less porous in the waterglass–AAS than in the other two materials. The dense microcracking was a result of the intense drying shrinkage in these materials.[41] The Ca/Si ratio of the gels formed was determined by EDS analysis in this area (at least 30 analyses per sample). The findings are given in Table 4.

Fig. 5 shows the Young's modulus and hardness histograms based on the measurements taken on AAS and OPC samples, from which a number of conclusions can be drawn (See also Table 5). Both mechanical properties exhibited more than one distribution pattern in all the samples, an indication that mechanical behaviour differs in different regions of cement materials. According to the histograms in Fig. 5(a–d), three general patterns were present. The existence of three mechanical states in OPC concurs with the general belief that C-S-H may exhibit low (LD), high (HD)[42] or ultra high (UHD) density states.[43] The present study shows for the first time that clearly differenciated mechanical states also exist in AAS C-A-S-H gels, which suggest that the density regimens are intrincis from the dissolution-precipitation process. The contour maps of Young's modulus in Fig. 6 were plotted after interpolating the results of the nanoindentation findings to locate representative microstructural areas. A distinct correlation was found between the microstructure visible in the BSE/SEM images (Fig. 6(a), (c) and (e)) and the mechanical contour maps (Fig. 6(b), (d) and (f)). In other words, mechanical behaviour varied with the microstructural characteristics of the samples.

Table 6
Numerical model values for structural parameters.

Model	Structural information				Elastic property			
	Chain length	Al/Si	Ca/Si	Q^3/Q^2	*E* (GPa)	*K* (GPa)	*G* (GPa)	nu
J	2	0	2.25	0.0	34.72	23.9	13.8	0.26
	5	0	1.8	0.0	46.27	31.8	18.4	0.26
T14	2	0	1.25	0.0	34.92	26.22	13.66	0.28
	5	0.18	1.18	0.0	56.35	40.68	22.2	0.27
	8	0.14–0.23	1.11–1.20	0.0	49.85	35.26	19.75	0.26
	11	0.16–0.22	1.05–1.11	0.0	49.52	36.24	19.46	0.27
T11	2	0	1.00	0.0	32.24	22.25	12.81	0.26
	5	0.18	0.94	0.20	64.00	55.05	24.5	0.31
	8	0.14–0.23	0.86–0.92	0.25	71.82	60.66	27.57	0.30
	11	0.16–0.22	0.84–0.89	0.27	69.44	68.34	26.10	0.33
	14	0.17–0.22	0.83–0.85	0.28	74.03	66.91	28.13	0.32

4.2. Atomistic simulation

C-S-H structural models vary depending on the Ca/Si ratio. At the Ca/Si values typical of OPC (1.5–2.2), the gel comprises imperfect and short (dimeric and pentameric) tobermorite 1.4 nm- and jennite-like configurations. The two chief changes observed, consistently confirmed by NMR experiments, are that a decrease in the Ca/Si ratio implies an increase in mean chain length and the appearance of Q^3 sites. This would explain why other structural analogues such as tobermorite 1.1 nm have also been suggested as models[14,44] for materials with low Ca/Si ratios. Interestingly, the effect of Al atom uptake into the C-A-S-H gel structure generates similar changes, for several experiments[31–33] and simulations[29] have shown that the Al atoms also lengthen the chains and prompt the appearance of a three-dimensional structure. Inasmuch as the C-A-S-H gels in AAS have higher Al/Si and lower Ca/Si ratios than OPC, tobermorite 1.1 nm, in addition to the 1.4 nm polymorph, clearly constitutes a structural model worth exploring. As noted in Section 3, many tobermorite 1.1 nm and 1.4 nm structures have been built with different Al/Si ratios and mean chain lengths. Fig. 7 contains a few examples by way of illustration, while Table 6 lists the values of the structural parameters analysed.

4.2.1. Effect of silicate mean chain length on Young's modulus

Several atomistic simulations have shown the Young's modulus (E) for perfect tobermorite 1.1 nm and 1.4 nm to be 77.3 and 49.9 GPa, respectively, in the absence of Al replacements for Si.[15,22,23] The greater elasticity in tobermorite 1.1 nm may be attributed to the higher inter-layer cohesion provided by the bonding between bridging tetrahedral of consecutive layers. This contribution of the interlaminar covalent bonds to elasticity can also be seen by plotting E values versus chain length. Fig. 8a shows that the Young's modulus values for both tobermorite polymorphs rise with increasing mean chain length and tend to converge at infinity for large chains. The shortening of the aluminosilicate process by removing one bridging tetrahedron induces defects in the crystalline structure and with them a concomitant decline in elasticity. One interesting fact is that while for dimers elasticity is similar in the two varieties of tobermorite, in longer chains where interlaminar covalent bonding comes into play, tobermorite 1.1 nm exhibits higher E values than the 1.4-nm polymorph.

4.2.2. Effect of aluminium atom uptake

The elastic properties values in Table 6 refer to Al-free structures. The present simulations showed that substituting Al for Si had no significant effect on elasticity, however. According to these findings, in tobermorite 1.1 and 1.4 nm both, the dispersion around the mean bulk, shear and Young's modulus values for a given chain length was under 6 GPa, regardless of the Al/Si ratio. This invariability is illustrated in Fig. 8b, where Young's modulus for T11 (8) and T14 (8) are plotted against the Al/Si ratio. The negligible effect of replacing Si with Al on elasticity can be readily justified in terms of the similar strength of the Si–O–Si and Al–O–Si bonds and the key role of the interlaminar forces.

5. Discussion: a model for C-A-S-H nanostructure

Further to the mineralogical and structural characterisation conducted on OPC and AAS pastes, the C-S-H and C-A-S-H gels forming in these pastes, cured under the same conditions and for the same length of time, exhibited substantial mineralogical and structural differences, findings which concurred with prior reports.[10,38] The C-S-H gel forming in OPC pastes had a chain-like structure and was characterised by a low Al content, low $\Sigma Q^2/Q^1$ ratios and a mean chain length (MCL) of three to five tetrahedra (see Table 7). Differences in gel structure were observed in the AAS pastes depending on the nature of the alkali activator. When it was an NaOH solution, the C-A-S-H gel contained Al in its composition (in chain bridging positions) and exhibited a high Q^2 (1Al) content, low Q^3 unit percentages, an MCL of nine and high $\Sigma Q^2/Q^1$ ratios. When a waterglass solution was used as the activator, the C-A-S-H gel formed had high percentages of Al, high $\Sigma Q^2/Q^1$ ratios, a higher Q^3 unit content and a mean chain length of around 11 tetrahedra. The presence of Q^3 units in the AAS gels was an indication of intertwining between the gel chains, with the formation of laminar structures

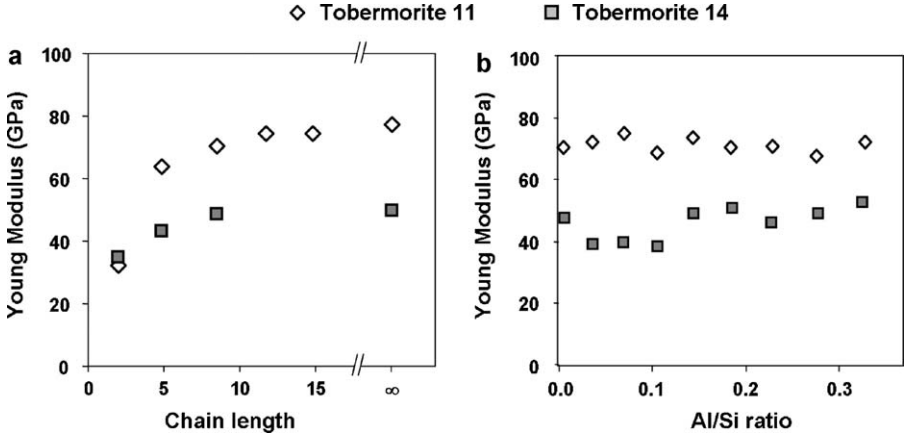

Fig. 8. Effect of (a) MCL and (b) the Al/Si ratio on Young's modulus for T11 and T14.

Table 7
Data obtained form ^{29}Si MAS NMR signal deonvolution values.

Paste	MCL	$\Sigma Q^2/Q^{total}$	Q^2 (0Al)/Q^2 (1Al)	$\Sigma Q^2/Q^1$	Al/Si
CEM 28 days	3.80	0.47	–	0.90	–
EW 28 days	12.71	0.71	0.62	3.70	0.24
EN 28 days	8.00	0.70	0.62	2.84	0.23

in some areas. The BSEM/EDS findings confirmed the FTIR and NMR results, for longer, intertwined chains of silicate tetrahedra lower the Ca/Si ratio in these gels. The results given in Table 4 show that while the Ca/Si ratio in the OPC paste C-S-H gel was 2.19 ± 0.22, the value of this parameter declined to 1.10 ± 0.11 in the C-A-S-H gel found in NaOH–AAS (EN-AAS) and to 0.96 ± 0.10 in the waterglass–AAS (Wg-AAS) material. In other words, increasing the Al content in the gel raised the mean chain length, favoured linear chain intertwining and lowered the Ca/Si.

From the standpoint of mechanical performance, the nanoindentation studies showed that, as in C-S-H gel, C-A-S-H gel had distinct mechanical states. Nonetheless, the structural and compositional differences in C-S-H and C-A-S-H gels translated into differences in their moduli of elasticity and hardness. The data in Fig. 5 show that the highest strength values were obtained for Waterglass-AAS gels, followed by the OPC gels and finally the NaOH-AAS gels. This lower strength in the NaOH-AAS pastes may be explained by the much higher porosity found in these pastes than in the waterglass–AAS materials, as confirmed by the BSEM.

A correlation of the computational results found in this study to the experimental data on chemical composition, silicate chain structure and nanoindentation elasticity leads fairly straightforwardly to a suggested structural model for C-S-H and C-A-S-H gels. The C-S-H gel forming in OPC pastes may be described as an imperfect tobermorite 1.4 nm. The difference in the Ca/Si ratio, which is lower in defective tobermorite 1.4 nm than in C-S-H gel, may be attributed to the co-existence of jennite-like structures in the latter, whose Ca/Si ratios have been suggested to be much higher (up to 2.2) in prior empirical and theoretical studies. The C-S-H samples analysed here, with an experimental MCL value of 3.8, may be regarded to comprise 60% T14 (5) and 40% J (2). Note that this population of T14 (5) and J (2) concurs very reasonably with the experimental values found for the Ca/Si, Al/Si and Q^3/Q^2 ratios (see Table 7). Table 8 also gives the intrinsic elastic properties of a C-S-H gel consisting of 60% T14 (5) and 40% J (2). As mentioned above, since the nanoindentation measurements also reflect porosity-related effects, they cannot be directly correlated to the values in Table 8. A self-consistent (SC) micromechanical model was consequently used to incorporate the effect of porosity on elastic properties and thereby establish a more significant correlation. Fig. 9 plots the Young's modulus calculated with the model (dots) against packing efficiency (ϕ). The coloured bands in the figure depict the dispersion around the mean values (stars) in distributions A, B and C.

The existence of three mechanical states is consistent with prior studies[43] that relate these states in C-S-H gel to packing density: LD, HD and UHD. Moreover, as Fig. 9 shows, the numerical results accurately predict C-S-H particle packing factors. The states corresponding to distribution patterns A, B and C can be readily associated with the LD, HD and UHD varieties, respectively. The present study yielded packing factors for the C-S-H states defined of around 0.68, 0.77 and 0.9, which concur extremely well with the estimates provided previously,[42,43] namely 0.69 ± 0.05, 0.78 ± 0.02 and 0.89 ± 0.03. LD varieties are normally regarded to be random C-S-H particles, since the random limit packing factor of spherical particles is 0.64.[45] The packing factors for the HD varieties are similar to the packing factors for ordered face-centred cubic (fcc) or hexagonal close packed (hcp) spheres (0.74). The extremely high packing factor corresponding to the UHD states cannot be explained in terms of single spherical particles. Vandamme et al.[43] maintained that this factor would be due to random packing of two spherical particle classes ($1 - (1 - 0.64)^2$). Interestingly, Ref. 47 explains the nature of the UHD state as arising from an intimate nanocomposite where nanoscale Portlandite reinforces C-S-H by partially filling the latter's gel pores, something which matches well with the aforementioned interpretation based on a biphase mixture of spheres.[43] The existence of the three regimens for different systems indicates that the packing density is an intrinsic characteristic of the hydration reactions. Different packing densities arise from the available space, with looser packing far from the clinker or fly ash particles, and tighter packing close to them.

The Ca/Si ratio and the percentage of Q^3 sites in the C-A-S-H gel formed in NaOH-AAS suggest that its atomic scale structure might be close to the tobermorite 1.1-nm model. Given the experimental mean chain length, Ca/Si, Al/Si and Q^3/Q^2 ratios, these C-A-S-H varieties might well be described to contain a

Table 8
Model values.

Model	MCL	Ca/Si	Al/Si	Q3/Q2	*E*	*G*	*K*	nu
OPC (J2 + T5)	3.8	1.96	0.0	0.0	47.7	18.84	33.83	0.27
EN 67% T14 (5) + 33% T11 (14)	8.0	1.05	0.185	0.09	62.18	24.15	48.73	0.29
EW 44% T14 (11) + 56% T11 (14)	12.4	0.95	0.193	0.15	70.8	26.9	82.31	0.36

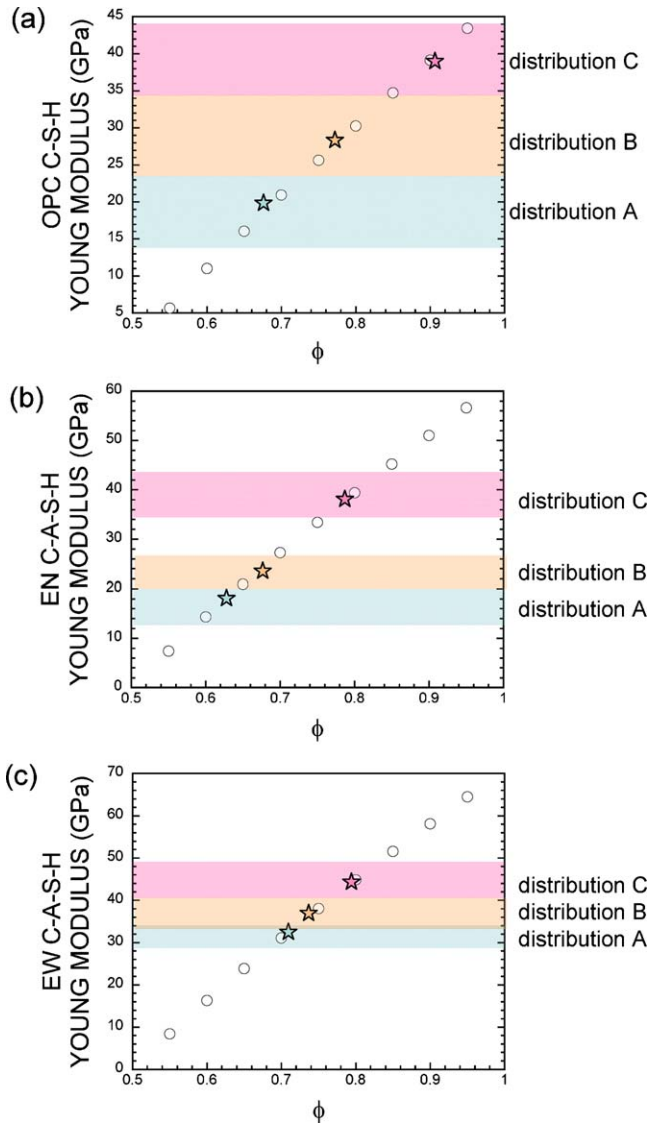

Fig. 9. Porosity versus Young's modulus for OPC C-S-H, EN C-A-S-H and EW C-A-S-H.

mix of T14 (5) and T11 (14) components. Assuming the T14 (5) and T11 (14) populations to account for 67 and 33%, respectively, of the total concurs reasonably well with the experimental observations. While the intrinsic values of the elastic properties are higher in NaOH-AAS C-A-S-H particles than in the C-S-H present in OPC (see Table 8), the former ultimately perform poorly, an obvious result of their high porosity. Fig. 9 shows that the three mechanical regions can be attributed to NaOH-AAS C-A-S-H particles with packing factors of around 0.63, 0.68 and 0.79. The first two states fall within category LD (similar to the random packing limit), whereas the third indisputably lies within what may be regarded to be an HD state. Unlike OPCs, EN C-A-S-H gels cannot exist in the UHD state because NaOH-AAS have no portlandite, which is essential to the existence of that state.[46]

When the activator is waterglass, an educated suggestion would be that these varieties of C-A-S-H are a mix of T14 (11) and T11 (14) configurations. Under that assumption, relative populations of the two structural models of 44 and 56%, respectively, concur well with the experimental results (se Table 8). Waterglass-AAS C-A-S-H gels exhibit better intrinsic properties than the other two materials (see Table 8) as a result of their high relative T11 population. Furthermore, the SC micromechanical model findings (see Fig. 9) corroborate the nanoindentation results: these gels form a very dense structure. As Fig. 9 shows, Waterglass-AAS C-A-S-H gels exhibit three mechanical states, with packing factors of 0.71, 0.73 and 0.79. Given the proximity of these values to the factor for the HD category, they were classified accordingly. The EW C-A-S-H gels, like their EN counterparts, have no UHD states as a result of the absence of portlandite.

6. Conclusions

The conclusions to be drawn from the findings reported and analysed above are as follows.

1. The C-S-H and C-A-S-H gels forming in OPC and AAS pastes exhibit compositional and structural differences. The former is characterised by a chain-like structure, a low Al content and low $\Sigma Q^2/Q^1$ ratios and a mean chain length of three to five tetrahedra. In the AAS pastes, the C-A-S-H gels formed exhibit structural differences depending on the nature of the alkali activator. When it is an NaOH solution, the C-A-S-H gel contains Al in its composition (in bridge positions) and has a high $Q^2(1Al)$ content, low Q^3 unit percentages, an MCL of nine and high $\Sigma Q^2/Q^1$ ratios. When a waterglass solution is used as the activator, the C-A-S-H gel formed has high percentages of Al in tetrahedral positions, high $\Sigma Q^2/Q^1$ ratios, a higher Q^3 unit content and a mean chain length of around 11 tetrahedra. The presence of Q^3 units in the AAS gels is an indication of the gel chain intertwining, with the formation of laminar structures in some areas.
2. Modulus of elasticity and hardness values were determined for the gels formed in the OPC pastes, and for the first time for the gels present in AAS pastes, with nanoindentation trials. The values vary depending on the compositional and structural characteristics of the gels. The present experimental study showed for the first time that like the C-S-H gel in OPCs, the C-A-S-H in AAS can be found in different mechanical states. This suggests that the presence of difference packing efficiencies is intrinsic from the hydration reactions.
3. The tobermorite structures on which the C-A-S-H gels in AAS pastes can be patterned were established for the first time, and compared to the gel in an OPC paste, using experimentally validated modelling techniques.

3.1 The C-S-H gel in a 28-day OPC paste corresponds primarily to tobermorite 14 nm (mean chain length of five tetrahedra) and jennite (two tetrahedra). The mechanical properties of C-S-H gels can be explained on the grounds of three types of packing, i.e., LD, HD and UHD.

3.2 The structure of a C-A-S-H gel obtained in 28-day NaOH-AAS pastes can be regarded to fall in between tobermorite

1.4 nm with a mean chain length of five and tobermorite 1.1 nm with a mean length of 14 tetrahedra. The high porosity induced by the molecular disorder explains the scant elasticity of the gel forming under these conditions, which comprises primarily LD-type states. Although a small population of HD states is present in the gel, the absence of portlandite prevents the formation of UHD states.

3.3 In C-A-S-H gels forming in 28-day waterglass-AAS, the structure found for the C-A-S-H gel formed is indicative of the co-existence of tobermorite 1.4 nm, with a chain length of 11, and tobermorite 1.1 nm, with a chain length of 14 tetrahedra. This very densely packed structure (three HD states) gives rise to excellent mechanical properties. Like the C-A-S-H gels obtained in NaOH-AAS paste, the C-A-S-H gels forming in waterglass-AAS gels have no UHD states.

Acknowledgements

This research was funded by the European Union under contract NMP3-SL-2008-214030 and the Spanish Ministry of Science and Innovation under project BIA2007-61380. M. Palacios participated under a postdoctoral contract awarded by the Spanish National Research Council. H. Manzano acknowledges the grant received from the Basque Government through the "Improvement of Research Staff" program of the Education, University and Research Department.

References

1. Fernández-Jiménez A, Puertas F, Palomo JG. Alkali-activated slag mortars: mechanical strength behaviour. *Cement and Concrete Research* 1999;**29**:593–604.
2. Brough AR, Atkinson A. Sodium silicate-based, alkali-activated slag mortars. Part I. Strength, hydration and microstructure. *Cement and Concrete Research* 2002;**32**:865–79.
3. Bakharev T, Sanjayan JG, Cheng Y-B. Sulfate attack on alkali-activated slag concrete. *Cement and Concrete Research* 2002;**32**:211–6.
4. Bakharev T, Sanjayan JG, Cheng Y-B. Resistance of alkali-activated slag concrete to acid attack. *Cement and Concrete Research* 2003;**33**:1607–11.
5. Puertas F, Mejía de Gutierrez R, Fernández-Jiménez A, Delvasto S, Maldonado J. Alkaline cement mortars. Chemical resistance to sulfate and seawater attack. *Materiales de Construccion* 2002;**52**(267):55–71.
6. Puertas F, Palacios M, Vázquez T. Carbonation process of alkali-activated slag mortars. *Journal of Materials Science* 2006;**41**:3071–82.
7. Bakharev T, Sanjayan JG, Cheng Y-B. Resistance of alkali-activated slag concrete to carbonation. *Cement and Concrete Research* 2001;**31**:1277–83.
8. Palacios M, Puertas F. Carbonation of alkali-activated slag pastes. *Journal of American Ceramic Society* 2006;**89**(10):3211–21.
9. Palacios M, Puertas F. Influence of shrinkage-reducing admixture on the properties of alkali-activated slag mortars and pastes. *Cement and Concrete Research* 2007;**37**:691–702.
10. Fernández-Jiménez A, Puertas F, Sobrados I, Sanz J. Structure of calcium silicate hydrates formed in alkaline activated slag. Influence of the type of alkaline activator. *Journal of American Ceramic Society* 2003;**86**(3):1389–94.
11. Lecomte I, Henrist C, Líegeois M, Maseri F, Rulmont A, Cloots R. (Micro)-structural comparison between geopolymers, alkali-activated slag cement and Portland cement. *Journal of the European Ceramic Society* 2006;**26**:3789–97.
12. Richardson IG. The calcium silicate hydrates. *Cement and Concrete Research* 2008;**38**:137–58.
13. Puertas F, Fernández-Jiménez A, Blanco-Varela MT. Pore solution in alkali-activated slag cement pastes. Relation to the composition and structure of calcium silicate hydrate. *Cement and Concrete Research* 2004;**34**:139–48.
14. Dolado JS, Griebel M, Hamaekers J. A molecular dynamic study of cementitious calcium silicate hydrate (C-S-H) gels. *Journal of American Ceramic Society* 2007;**90**(12):3938–42.
15. Manzano H, Dolado JS, Ayuela A. Structural and elastic properties of the main species present in the cement paste. *Acta Materialia* 2009;**57**(5):1666–74.
16. Pellenq RJ-M, Kushima A, Shahsavari R, Van Vliet KJ, Buehler MJ, Yip S, Ulm F-J. A realistic molecular model of cement hydrates. *Proceedings of the National Academy of Sciences* 2009;**106**(38):16102–7.
17. Constantinides G, Ulm FJ. The nanogranular nature of C-S-H. *Journal of the Mechanics and Physics of Solids* 2007;**55**:64–90.
18. Leach AR. *Molecular modelling: principles and applications*. 2nd ed. England/New York: Harlow/Prentice Hall; 2001, xxiv, 744 p., [16] p. of plates.
19. Gmira A, et al. Microscopic physical basis of the poromechanical behavior of cement-based materials. *Materials and Structures* 2004;**37**(265):3–14.
20. Lewis GV, Catlow CRA. Potential models for ionic oxides. *Journal of Physics C-Solid State Physics* 1985;**18**(6):1149–61.
21. Du ZM, de Leeuw NH. A combined density functional theory and interatomic potential-based simulation study of the hydration of nano-particulate silicate surface. *Surface Science* 2004;**554**(2–3): 193–210.
22. Manzano H, González-Teresa R, Dolado JS, Ayuela A. X-ray spectra and theoretical elastic properties of crystalline calcium silicate hydrates: comparison with cement hydrated gels. *Materiales de Construcción* 2010;**60**(299):7–19.
23. Manzano H, Dolado JS, Guerrero A, Ayuela A. Mechanical properties of crystalline calcium-silicate-hydrates: comparison with cementitious C-S-H gels. *Journal Physica Status Solidi a-Applications and Materials Science* 2007;**204**(6):1775–80.
24. Gale JD, Henson NJ. Derivation of interatomic potentials for microporous aluminophosphates from the structure and properties of berlinite. *Journal of the Chemical Society-Faraday Transactions* 1994;**90**:3175–9.
25. Higgins FM, de Leeuw NH, Parker SC. Modelling the effect of water on cation exchange in zeolite A. *Journal of Materials Chemistry* 2002;**12**(1):124–31.
26. Bonaccorsi E, Merlino S, Kampf AR. The crystal structure of tobermorite 14 A (Plombierite), a C-S-H phase. *Journal of American Ceramic Society* 2005;**88**(3):505–12.
27. Merlino S, Bonaccorsi E, Armbruster T. The real structure of tobermorite 11 angstrom: normal and anomalous forms, OD character and polytypic modifications. *European Journal of Mineralogy* 2001;**13**(3):577–90.
28. Manzano H, Dolado JS, Ayuela A. Aluminum incorporation to dreierketten silicate chains. *Journal of Physical Chemistry B* 2009;**113**(9), 2832-283912.
29. Manzano H, Dolado JS, Griebel M, Hamaekers J. A molecular dynamics study of the aluminosilicate chains structure in Al-rich calcium silicate hydrated (C-S-H) gels. *Physica Status Solidi a-Applications and Materials Science* 2008;**205**(6):1324–9.
30. Sun GK, Young JF, Kirkpatrick RJ. The role of Al in C-S-H: NMR XRD, and compositional results for precipitated samples. *Cement and Concrete Research* 2006;**36**(1):18–29.
31. Richardson IG, Brough AR, Brydson R, Groves GW, Dobson CM. Location of aluminium in substituted calcium silicate hydrate (C-S-H) gels as determined by Si-29 and Al-27 NMR and EELS. *Journal of the American Ceramic Society* 1993;**76**(9):2285–8.
32. Andersen MD, Jakobsen HJ, Skibsted J. Incorporation of aluminum in the calcium silicate hydrate (C-S-H) of hydrated Portland cements: a high-field Al-27 and Si-29 MAS NMR. *Inorganic Chemistry* 2003;**42**(7):2280–7.
33. Faucon P, Charpentier T, Nonat A, Petit JC. Incorporation of aluminum in the calcium silicate hydrate (C-S-H) of hydrated Portland cements: a high-field Al-27 and Si-29 MAS NMR. *Journal of the American Chemical Society* 1998;**120**(46):12075–82.
34. Gale JD, Rohl AL. The general utility lattice program (GULP). *Molecular Simulation* 2003;**29**(5):291–341.

35. Kröner E. *Statistical continuum mechanics*. New York: Springer-Verlag; 1972.
36. Kirkpatrick RJ, Cong YX. An in introduction to ^{27}Al and ^{29}Si NMR spectroscopy of cements and concretes. In: Colomet P, Grimmer A, editors. *Application of NMR spectroscopy to cement science*. 1994. p. 55–76.
37. Cincotto MA, Melo AA, Repette WL. Effect of different activators type and dosages and relation to autogenous shrinkage of activated blast furnace slag cement. In: *Proceedings of the 11th International Congress on the Chemistry of Cement (ICCC) Cements Contribution to the Development in the 21st Century*. 2003. p. 1878–88.
38. Skibsted J, Jakobsen HJ, Hallt C. Quantitative aspects of ^{27}Al MAS NMR of calcium aluminoferrites. *Advances in Cement Based Materials* 1998;**7**:57–9.
39. Brunet F, Charpentier T, Chao CN, Peycelon H, Nonat A. Characterization by solid-state NMR and selective dissolution techniques of anhydrous and hydrated CEM V cement pastes. *Cement and Concrete Research* 2010;**40**:208–19.
40. Oldfied E, Kinsey RA, Smith KA, Nichols JA, Kirkpatrick RJ. High-resolution NMR of inorganic solids. Influence of magnetic centers on magic-angle sample-spinning lineshapes in some natural aluminosilicates. *Journal Magnetic Resonance* 1983;**51**:325–9.
41. Palacios M. *Empleo de aditivos orgánicos en la mejora de las propiedades de cementos y morteros de escorias activadas alcalinamente* (*Spanish*). PhD. Autonoma University of Madrid; 2006.
42. Constantinidis G, Ulm F-JJ. The nanogranular origin of C-S-H. *Journal of the Mechanics and Physics of Solids* 2007;**55**:64–90.
43. Vandamme M, Ulm F-J. Nanogranular of concrete creep. *Proceedings of the National Academy of Sciences of the United States of America* 2009;**106**:10552.
44. Skinner LB, Chae SR, Benmore CJ, Wenk HR, Monteiro PJM. Nanostructure of calcium silicate hydrates in cements. *Physical Review Letters* 2010;**104**:195502.
45. Song C, Wang P, Makse HA. A phase diagram for jammed matter. *Nature* 2008;**453**(7195):629–32.
46. Chen JJ, Sorelli L, Vandamme M, Ulm J-F, Chanvillard G. A coupled nanoindentation/SEM-EDS study on low water/cement ratio portland cement paste: evidence for C-S-H/Ca(OH)$_2$ nanocomposites. *Journal of American Ceramic Society* 2010;**93**(5):1484–93.
47. de Leeuw NH, Watson GW, Parker SC. Atomistic simulation of the effect of dissociative adsorption of water on the surface structure and stability of calcium and magnesium oxides. *Journal of Physical Chemistry* 1995;**99**(47):17219–25.
48. De Leeuw NH, Parker SC. Molecular-dynamics simulation of MgO surfaces in liquid water using a shell-model potential for water. *Physical Review B* 1998;**59**:13901–8.
49. Schroder KP, et al. Bridging hydroxyl groups in zeolitic catalysts: a computer simulation of their structure, vibrational properties and acidity in protonated faujasites (HY zeolites). *Chemical Physics Letters* 1992;**188**(3–4):320–5.